MNRAS 000, 1–7 (2016) Preprint 1 December 2016 Compiled using MNRAS LATEX style file v3.0

Features of collisionless turbulence in the intracluster medium from simulated Faraday rotation maps II: the effects of instabilities feedback

R. Santos-Lima,[1⋆] E. M. de Gouveia Dal Pino,[1] D. A. Falceta-Gonçalves,[2] M. S. Nakwacki,[3,4] and G. Kowal[5,2]

[1] *Instituto de Astronomia, Geofísica e Ciências Atmosféricas, Universidade de São Paulo, R. do Matão, 1226, São Paulo, SP 05508-090, Brazil*
[2] *Escola de Artes, Ciências e Humanidades, Universidade de São Paulo, São Paulo, SP, Brazil*
[3] *Instituto de Astronomía y Física del Espacio, UBA-CONICET, Argentina*
[4] *Facultad de Ciencias Exactas y Naturales, Universidad de Buenos Aires, Argentina*
[5] *Núcleo de Astrofísica Teórica, Universidade Cruzeiro do Sul, São Paulo, SP, Brazil*

Accepted XXX. Received YYY; in original form ZZZ

ABSTRACT

Statistical analysis of Faraday Rotation Measure (RM) maps of the intracluster medium (ICM) of galaxy clusters provides a unique tool to evaluate some spatial features of the magnetic fields there. Its combination with numerical simulations of magnetohydrodynamic (MHD) turbulence allows the diagnosis of the ICM turbulence. Being the ICM plasma weakly collisional, the thermal velocity distribution of the particles naturally develops anisotropies as a consequence of the large scale motions and the conservation of the magnetic moment of the charged particles. A previous study (Paper I) analyzed the impact of large scale thermal anisotropy on the statistics of RM maps synthesized from simulations of turbulence; these simulations employed a collisionless MHD model which considered a tensor pressure with uniform anisotropy. In the present work, we extend that analysis to a collisionless MHD model in which the thermal anisotropy develops according to the conservation of the magnetic moment of the thermal particles. We also consider the effect of anisotropy relaxation caused by the micro-scale mirror and firehose instabilities. We show that if the relaxation rate is fast enough to keep the anisotropy limited by the threshold values of the instabilities, the dispersion and power spectrum of the RM maps are indistinguishable from those obtained from collisional MHD. Otherwise, there is a reduction in the dispersion and steepening of the power spectrum of the RM maps (compared to the collisional case). Considering the first scenario, the use of collisional MHD simulations for modeling the RM statistics in the ICM becomes better justified.

Key words: magnetic fields – turbulence – methods: numerical – galaxies: clusters: intracluster medium

1 INTRODUCTION

Cosmological mergers of galaxy clusters, AGN jets, galactic winds, and galaxy interactions drive turbulence in the plasma filling the intracluster medium (ICM), and this turbulence would be able to amplify weak seeds of magnetic fields up to intensities of $\sim \mu G$, according to cosmological magneto-hydrodynamical (MHD) simulations (e.g. Kotarba et al. 2011; Beresnyak & Miniati 2016; Egan et al. 2016). This amplification mechanism could explain the magnetic fields detected in the diffuse ICM through synchroton emission of relativistic electrons in radio halos, and also through the Faraday rotation of polarized emission from radio sources embedded or behind the galaxy clusters (see Brunetti & Jones 2014 and references therein). In fact, two-point statistics of the Faraday rotation maps of the ICM reveal a magnetic field power spectrum consistent with a Kolmogorov-like power law $\propto k^{-5/3}$ (Enßlin, Vogt, & Pfrommer 2005).

However, the use of the standard MHD approximation to describe the dynamics of the ICM and the development of the small-scale turbulent dynamo is, in prin-

⋆ E-mail: rlima@astro.iag.usp.br

ciple, not well justified since it implies a high collisionality of the plasma particles to ensure the local thermodynamical equilibrium. Considering that the mean-free-path for the ion-ion Coulomb collisions is typically $\lambda_{ii} \sim 30$ kpc in the ICM (considering a density $n = 10^{-3}$ cm^{-3} and temperature $T = 10^8$ K; see also the ion mean-free-path distribution inferred from cosmological simulations in Egan et al. 2016), collisionless effects should be taken into account at least for scales $\lesssim \lambda_{ii}$ (see Schekochihin & Cowley 2006). The most obvious effect is the natural development of pressure (or temperature) anisotropy with respect to the local magnetic field. As a consequence there is the triggering of electromagnetic plasma instabilities (such as the firehose, the ion-cyclotron and the mirror instabilities; see, e.g., Gary 1993). These instabilities are known to constrain the anisotropy itself (see Santos-Lima et al. 2014 and references therein; Kunz, Schekochihin, & Stone 2014; Riquelme, Quataert, & Verscharen 2015; Sironi & Narayan 2015; Sironi 2015; Rincon, Schekochihin, & Cowley 2015; Melville, Schekochihin, & Kunz 2016; Santos-Lima et al. 2016).

Santos-Lima et al. (2014, SL+14 hereafter) took into account some collisionless effects in numerical simulations of turbulence and small-scale dynamo in MHD numerical simulations considering the conditions typical of the ICM. They found that under forced turbulence, the perpendicular temperature to the local magnetic field dominates the parallel temperature in most of the system (the parallel temperature dominates only in narrow regions of high compression or magnetic field reversals), leading to strong modifications in the turbulence statistics (see also Kowal, Falceta-Gonçalves, & Lazarian 2011; Falceta-Gonçalves & Kowal 2015 for studies on collisionless turbulence with constant pressure anisotropy) and the complete failure of the dynamo. On the other hand, including the relaxation of the temperature anisotropy resulting from the microscale (scales below those resolved in the simulation, down to the ions kinetic scales) plasma instabilities, the system gradually converges to a similar behaviour to that obtained by collisional MHD, depending on the anisotropy relaxing rate [1]. In SL+14 it is argued that this relaxing rate is much faster than the MHD time-scales, and the model that better represents the ICM constrains the maximum anisotropy levels to values very close to the plasma stable regime.

The imprints of the large scale (of the order of turbulence injection scale) temperature anisotropy on the Faraday rotation maps were first studied in Nakwacki et al. (2016, Paper I hereafter). In that work, we employed a collisionless MHD formalism with a double-isothermal closure (as implemented in Kowal, Falceta-Gonçalves, & Lazarian 2011) to analyse the statistical properties of the RM maps for several models of turbulence considering different values of the fixed temperature anisotropy and different regimes of sub/super-Alfvénic and trans/supersonic turbulence. The effects of the temperature anisotropy on the magnetic field structure and the RM maps were found to be significant evidencing smaller correlation lengths when compared to collisional MHD models. In that study it was neglected the feedback of the microscale instabilities on the plasma which may cause the reduction of the thermal anisotropy as described in SL+14 (see also Schekochihin & Cowley 2006).

In this work, we will extend the analysis of Paper I by including this effect. We will explore the collisionless effects on the Faraday rotation maps focusing on the turbulence models of the intracluster medium presented in SL+14, in which the anisotropy in temperature evolves according to the CGL closure (Chew, Goldberger, & Low 1956) modified to include an anisotropy relaxing term. The important advantage of this new approach is not to use the double-isothermal closure, in which the temperature anisotropy is a fixed constant. We will compare the RM maps and related statistical properties of two collisionless MHD models, one similar to the models of Paper I (i.e. without any anisotropy relaxation), and another including bounds in the anisotropy. We will also compare these with the Faraday rotation maps obtained from a standard collisional MHD model.

In Section 2 we describe the numerical simulations of the collisionless MHD models used for building the synthetic Faraday rotation maps, which are analysed in Section 3. In Section 4 we summarize our results and draw our conclusions.

2 NUMERICAL SIMULATIONS

Table 1 shows the most relevant parameters of the simulated models used to build the synthetic RM maps. The brackets $\langle\cdot\rangle$ denote an average over the domain and time (using the available snapshots of the simulations, considering time intervals larger than τ_{turb}, where $\tau_{turb} = L_{turb}/U_{turb}$ is the turbulence turn-over time, with L_{turb} and U_{turb} the scale and velocity of injection, respectively), when the turbulence has reached a statistically stationary state. The values listed in parenthesis are the statistical standard deviations which give an approximate idea about the spatial and temporal fluctuations of these quantities. [2] The first three models (*CGL1, BA1,* and *MHD1*) have the same initial uniform magnetic field with intensity B_0 and thermal speed c_{s0} (both shown in dimensionless code units; see below). The rms turbulent velocity is also similar in these models (column $\langle u^2\rangle$). The initial thermal speed is kept approximately constant by the use of a fast thermal relaxation (which represents the action of both radiative cooling and heat conduction; see more details below). The regimes of turbulence achieved for these three models are similar being slightly subsonic ($u_{rms} \lesssim c_{S0}$) and mildly super-Alfvenic ($\langle M_A\rangle \gtrsim 1$). From all the models studied in SL+14, only these three ones have simulation parameters which are similar to those of the super-Alfvenic simulations analysed in Paper I and thus can be more easily compared with this previous work. However, the ICM is observed to have very tangled magnetic fields (e.g. Feretti et al. 1995), which is

[1] It should be made clear that the anisotropy relaxation employed in SL+14 does not drive the pressure components to the isotropic state, but to the instabilities thresholds. Therefore, the similarity to the collisional MHD results is not trivial.

[2] The spatial/temporal statistical distributions of the fields listed in Table 1 are not Gaussian around the mean values. This becomes obvious from the fact that all the quantities are positive and some of the standard deviation values are larger than the mean values.

Table 1. Parameters and statistics of the simulations used to build the synthetic RM maps.

run	B_0^2	c_{S0}^2	$\langle u^2 \rangle$	$\langle B^2 \rangle$	$\langle \beta \rangle$	$\langle M_A \rangle$	res.	snapshots
CGL1	0.09	1	0.59(0.54)	0.25(0.35)	$17(4.8 \times 10^2)$	1.8(1.3)	512^3	4
BA1	0.09	1	0.48(0.40)	0.51(0.33)	$16(4.8 \times 10^2)$	1.2(1.5)	512^3	4
MHD1	0.09	1	0.55(0.48)	0.58(0.47)	$17(9.4 \times 10^2)$	1.3(1.5)	512^3	4
CGL2	10^{-6}	1	0.70(0.73)	$1.2 \times 10^{-5}(7.1 \times 10^{-5})$	$2.0 \times 10^6(4.7 \times 10^7)$	$5.9 \times 10^2(5.7 \times 10^2)$	256^3	11
CGL3	10^{-6}	0.09	0.79(0.64)	$2.0 \times 10^{-4}(7.5 \times 10^{-4})$	$1.2 \times 10^5(1.1 \times 10^7)$	$2.8 \times 10^2(4.2 \times 10^2)$	256^3	11
BA2	10^{-6}	1	0.78(0.63)	0.12(0.15)	$1.7 \times 10^2(6.2 \times 10^3)$	4.6(6.7)	256^3	11
MHD2	10^{-6}	1	0.79(0.63)	0.18(0.22)	$1.1 \times 10^2(2.5 \times 10^3)$	3.8(5.3)	256^3	11

indicative of a turbulence regime strongly super-Alfvenic. The remaining models presented in Table 1 (*CGL2, CGL3, BA2*, and *MHD2*) are simulations in which the initial uniform magnetic field is very weak, making the intensity of the ordered component of the magnetic field to be relatively small after the amplification of the tangled component via small-scale turbulent dynamo (see B_0^2 and $\langle B^2 \rangle$ for these models in Table 1). These four models have the same initial seed magnetic field and thermal speed, except for model *CGL3*, where a smaller thermal speed is used in order to test the dependence of the results with the plasma $\beta = p_{th}/p_{mag}$ parameter (where $p_{th} = (2p_\perp + p_\parallel)/3$ is the total thermal pressure and $p_{mag} = B^2/8\pi$ is the magnetic pressure).

The models MHD (*MHD1* and *MHD2*) have a single scalar thermal pressure and correspond to the standard collisional MHD model where the distribution of the thermal velocities is assumed to be isotropic. The models named CGL (*CGL1, CGL2*, and *CGL3*) have a thermal pressure tensor with two independent components related to two temperatures: one associated to the thermal velocity component parallel to the local magnetic field lines $T_\parallel$ and another to the thermal velocity component related to the gyromotions of the particles around the field $T_\perp$; these two temperatures evolve according to the CGL closure (Chew, Goldberger, & Low 1956) which is based on the conservation of the magnetic moment of the charged particles $d\left(T_\perp/B\right)/dt = 0$ and the assumption of conservation of the entropy (no heat exchange between the fluid elements) $d\left(T_\perp^2 T_\parallel/n^2\right)/dt = 0$ (where n is the density of particles) [3]. Finally, the models named BA (Bounded Anisotropy: *BA1* and *BA2*) differ from models CGL by the addition of a boundary in the temperature anisotropy. This boundary limits the temperature anisotropy by the threshold values of the firehose (for $A < 1$) and mirror (for $A > 1$) instabilities, where A is the temperatures ratio $A = T_\perp/T_\parallel$, mimicking the effect of an "instantaneous" relaxing of the anisotropy to the marginal values by the action of the microscale instabilities (see Sharma et al. 2006; SL+14 and references therein). An extended discussion on the applicability and limitations of this model to represent the ICM turbulence is presented in Santos-Lima et al. (2016).

[3] In fact the CGL closure was not rigorously adopted in SL+14. Instead, a conservative scheme for evolving the internal energy was used, while the evolution of the temperatures ratio followed the CGL prescription (see Eq. 1). This approach gives results nearly identical to those obtained using the CGL equations of state, but is numerically more robust. Besides, it allows the straight inclusion of the anisotropy relaxation term.

The equations describing the evolution of the models presented in Table 1 are (see also SL+14):

$$\frac{\partial}{\partial t}\begin{bmatrix} \rho \\ \rho\mathbf{u} \\ \mathbf{B} \\ e \\ A(\rho^3/B^3) \end{bmatrix} + \nabla \cdot \begin{bmatrix} \rho\mathbf{u} \\ \rho\mathbf{u}\mathbf{u} + \Pi_P + \Pi_B \\ \mathbf{u}\mathbf{B} - \mathbf{B}\mathbf{u} \\ e\mathbf{u} + \mathbf{u}\cdot(\Pi_P + \Pi_B) \\ A(\rho^3/B^3)\mathbf{u} \end{bmatrix} = \begin{bmatrix} 0 \\ \mathbf{f} \\ 0 \\ \mathbf{f}\cdot\mathbf{v} + \dot{w} \\ \dot{A}_S(\rho^3/B^3) \end{bmatrix}, \tag{1}$$

where ρ, $\mathbf{u}$, $\mathbf{B}$, $p_{\perp,\parallel}$ are the macroscopic variables density, velocity, magnetic field, and thermal pressures perpendicular/parallel to the local magnetic field, respectively; $e = p_\perp + p_\parallel/2 + \rho u^2/2 + B^2/8\pi$ (for the two-temperature models CGL and BA) is total energy density. For the *MHD* model, $e = 3p/2 + \rho u^2/2 + B^2/8\pi$. Π_P and Π_B are the thermal pressure and magnetic stress tensors, respectively, defined by $\Pi_P = p_\perp \mathbf{I} + (p_\parallel - p_\perp)\mathbf{b}\mathbf{b}$ for the two-temperature models and simply $\Pi_P = p\mathbf{I}$ for the *MHD* model, $\Pi_B = (B^2/8\pi)\mathbf{I} - \mathbf{B}\mathbf{B}/4\pi$, where $\mathbf{I}$ is the unitary dyadic tensor and $\mathbf{b} = \mathbf{B}/B$. An ideal equation of state relates each temperature with its respective pressure component, and an adiabatic exponent $\gamma = 5/3$ is used for the MHD models. In the source terms, $\mathbf{f}$ represents an external bulk force responsible for driving the turbulence, $\dot{w}$ gives the rate of change of the internal energy $w = (p_\perp + p_\parallel/2)$ of the gas due to heat conduction and radiative cooling, and $\dot{A}_S$ gives the rate of change of A due to the microscale instabilities [4]

The turbulence is injected by adding a random (but solenoidal) velocity field (delta correlated in time) to the gas at the end of each time-step. This velocity field is concentrated inside a spherical shell in the Fourier space of radius $k = 2.5$ (i.e, with characteristic wavelength $L_{turb} = L/2.5$, being L is the side of the cubic domain). We employed an artificial but simple thermal relaxation prescription, which brings the specific internal energy w^* to its initial value w_0^*

[4] Though the physical process relaxing the macroscopic temperature anisotropy is attributed to the ions anomalous scattering in this approach, it can also represent (with some limitations) the situation when the relaxation is not mediated by the instantaneous break of magnetic momentum, as it is the case of the mirror instability development under continuous driving of temperature anisotropy (Kunz, Schekochihin, & Stone 2014; Riquelme, Quataert, & Verscharen 2015; Rincon, Schekochihin, & Cowley 2015; Melville, Schekochihin, & Kunz 2016). See discussion in Santos-Lima et al. (2016).

at a rate $\nu_{th} = 5$ (in code units, which gives a characteristic time approximately 20 times faster than the turbulence turn-over time τ_{turb}) for the models presented in Table 1:

$$\dot{w} = -\nu_{th}(w^* - w_0^*)\rho. \quad (2)$$

The instantaneous anisotropy relaxation (represented by the source term $\dot{A}$) is implemented as follows: after the numerical integration of the equations at each time-step, the anisotropy is replaced, at each grid cell, by the marginally stable value, whenever this evolves to an unstable value beyond the threshold for the firehose or mirror instability (see more details regarding the source terms and the numerical methods employed in the simulations in SL+14). As the results presented in this work are dimensionless and the above equations do not carry any physical constant, it is not necessary to attribute physical dimensions to the models.

We did not use explicit viscous or resistive terms in the numerical simulations (except for a small resistivity that provides a dissipation very close to the numerical one in the *CGL1* model for numerical stability purposes) aiming at reducing the dissipation to the minimum value provided by the numerical scheme, in order to maximize the inertial range of the turbulence. For the methods used in these simulations, the dissipation range starts at scales of approximately 16 cells (inferred from the magnetic and velocity power spectra of the MHD simulations). Therefore, we cannot assess the dependence of the results with the Reynolds R and/or the magnetic Prandtl number Pm ($R \equiv L_{turb}U_{turb}/\nu$ and $Pm \equiv \eta/\nu$, where ν and η are the viscous and magnetic diffusivities, respectively). We estimate the Pm number as approximately equal to unit in all our simulations.

3 SYNTHETIC FARADAY ROTATION MAPS

The statistics of the turbulence (that is, one and two point statistics) of the models described in the previous Section was studied in detail in SL+14 where models *Amhd*, *A*2, *A*1, *Cmhd*, *C*2, *C*3, and *C*1 correspond to *MHD1, CGL1, BA1, MHD2, CGL2, CGL3*, and *BA*2, respectively.

Figure 1 presents the maps of the dimensionless Faraday rotation measurement (RM):

$$RM = \int_0^L n_e B_{LOS} dl, \quad (3)$$

normalized by $n_{e0}B_0L$ (where B_0 is the intensity of the mean magnetic field, n_{e0} is the average density of electrons and L is the length of the Faraday screen) for the models *CGL1, BA1*, and *MHD1*, calculated for an arbitrary line-of-sight (LOS) whose direction has angle $\theta = 45^\circ$ with the mean magnetic field. The last snapshot of the simulations (at $\approx 10\tau_{turb}$) were used for the calculations.

A visual inspection shows that the RM map of model *CGL1* presents fluctuations of smaller amplitude compared to the *MHD1* model. Model *BA1* on the other hand, has the RM map appearance similar to model *MHD1*.

Figure 2 shows the normalized values of the average (top) and dispersion (bottom) of RM as a function of the angle θ, for the mildly super-Alfvenic models. The maps were built using 20 values of θ equally spaced between $\theta = 0$ and 90°, and the statistical moments were averaged over maps built from the different snapshots available for each model. The two-temperature models develop excess of perpendicular pressure in most of the domain ($A > 1$), and larger anti-correlation between the magnetic and density fluctuations (when compared to the one-temperature collisional MHD model; see Figure 10 in SL+14). This enhanced anti-correlation is expected to lead to a net reduction of the rotation measure in the case of the *CGL1* model when compared to the *MHD1* model. However, this reduction is found to be small (only a few percent) for small angles θ in the top plot of Figure 2. For increasing angles θ, the mean RM for the *CGL1* model converges to values close to the MHD model. The model *BA1* has the RM mean value similar to the *MHD1* model for all angles.

Due to the dominance of the perpendicular temperature component in the *CGL1* model, the thermal stresses offer resistance to motions perpendicular to the local field lines then reducing the fluctuations of the magnetic fields. In consequence, the fluctuations of the RM produced by the magnetic field turbulence are also affected. The bottom panel of Figure 2 compares the normalized dispersion of RM for the three models. This relative dispersion of the *CGL1* is about 2 times smaller (for small θ) compared to the *MHD1* model, and this difference is smaller for larger values of θ. The inclusion of the fast anisotropy relaxation by the microscale instabilities (model *BA1*) makes this relative dispersion in RM very similar to the MHD model.

Figure 3 compares the power spectrum of the RM maps for the mildly super-Alfvenic models. For each model, the power spectrum is shown for different values of θ (from $\theta = 0$ to 90°). For wavenumbers approximately in the estimated inertial range ($5 < k < 30$) the slopes of the power spectrum for the different lines of sight are nearly the same. While the *BA1* model has almost indistinguishable power spectrum from the *MHD1* model, the model *CGL1* has less power in all scales and is slightly flatter. We also note that the RM spectrum of the *CGL1* model has a power law close to $k^{-8/3}$ (which is expected when only the magnetic field fluctuates, that is, the density fluctuations are negligible) and an unidimensional power spectrum $|B_k|^2 \propto k^{-5/3}$, while model *MHD1* has a slightly flatter slope at small k values and then becomes slightly steeper at larger k. The corresponding magnetic power spectrum is slightly flatter than the Kolmogorov power law $k^{-5/3}$ in our simulation as shown in Fig. 6 of SL+14; the same can be observed in a similar simulation presented in Paper I (Fig. 6 left panel, model Bext=1, cs=1). Compared to model *MHD1*, the slow decay of the dissipation range of model *CGL1* points to an accumulation of power at the small scales (which are not properly solved by our grid resolution) caused by the kinetic instabilities (Paper I).

We repeated the analysis above for the strongly super-Alfvenic models *CGL2, CGL3, BA2*, and *MHD2*. Naturally, for these models the turbulent component of the magnetic field dominates the uniform one. This implies that the statistics of the RM maps built from these models is generally independent of the adopted LOS (except for the value corresponding to the mean field). In fact the statistics of the CGL models RM maps keeps a marginal dependence on the LOS, as the turbulent magnetic field is not as amplified here as in the MHD case. Table 2 shows the statistical moments for RM averaged over maps with different LOS (using 20 values of θ uniformly spaced in the interval between 0 and 90°). The

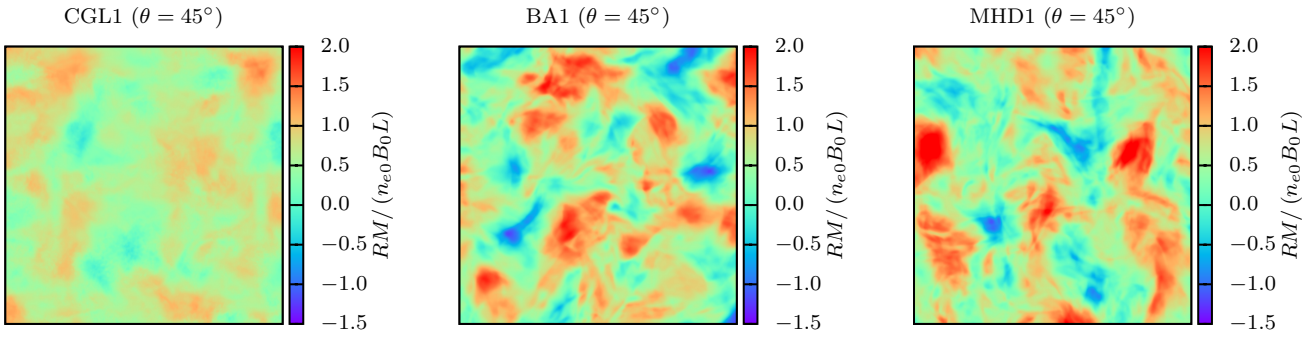

Figure 1. Normalized RM maps calculated from the simulated cubes: *CGL1* model with no anisotropy relaxing by the microscale instabilities (left), *BA1* with fast anisotropy relaxing by the instabilities (middle), and collisional *MHD1* model (right). The angle θ between the line-of-sight and the direction of the uniform magnetic field is 45° for all the maps.

Table 2. Statistical moments of the synthetic RM maps built from the strongly super-Alfvenic models.

run	$\langle \delta RM^2 \rangle / \left(n_{e0} B_{rms}^2 L\right)^2$	$\langle \delta RM^3 \rangle / \langle \delta RM^2 \rangle^{3/2}$	$\langle \delta RM^4 \rangle / \langle \delta RM^2 \rangle^2$
CGL2	1.6×10^{-2}	0.93	7.1
CGL3	2.5×10^{-2}	0.42	8.2
BA2	4.0×10^{-2}	3.6×10^{-2}	4.0
MHD2	3.6×10^{-2}	-8.5×10^{-3}	4.0

dispersion values $\langle \delta RM^2 \rangle$ are compared to $(n_{e0} B_{rms} L)^2$, in order to check how precisely we can track the intensity of the turbulent component of the magnetic field. Compared to the MHD model, the CGL models give a smaller value (by a factor of two), but this also depends on the compressibility of the turbulence, being slightly higher for the more compressible model *CGL3*. The model with bounds on the anisotropy *BA2* shows a dispersion similar to the MHD case. The skewness and kurtosis of the distribution of the RM are also shown in Table 2 (in columns $\langle \delta RM^3 \rangle / \langle \delta RM^2 \rangle^{3/2}$ and $\langle \delta RM^4 \rangle / \langle \delta RM^2 \rangle^2$, respectively). While model *BA2* presents results very similar to *MHD2*, with nearly zero skewness and the same values for the kurtosis, the CGL models show a positive skewness (which means a longer tail of large values) and a kurtosis approximately twice that of the MHD model, so that the distribution being is more peaked.

Figure 4 shows the power spectrum of RM for the highly super-Alfvenic models (averaged over the different LOS). The curves for the CGL models are displaced in the vertical axis and the values are multiplied by a factor of 100 in order to make the difference of the slopes between the models better observed. Similar to the mildly super-Alfvenic case, the CGL models present a flatter spectrum at large k values of the inertial range compared to the standard MHD model. The slope for model *CGL2* is even flatter than $k^{-8/3}$ (due to the increase of the small scale magnetic fluctuations caused by the instabilities which are stronger in this high beta plasma regime compared to the previous mildly super-Alfvenic case), while the *MHD2* model exhibits a power similar to the mildly super-Alfvenic case.

4 SUMMARY AND CONCLUSIONS

In this work we explored the role of plasma collisionless effects on simulated Faraday rotation maps resembling the conditions of the intracluster medium of galaxies (ICM). We presented a statistical analysis of the Faraday rotation maps obtained from simulations of forced turbulence in a three-dimensional domain with periodic boundaries considering three different models of the ICM plasma. The first one-temperature collisional MHD model considers isotropy in the velocity thermal distribution of the particles, an assumption that is not suitable *a priori* for the weakly collisional ICM, where the mean free path for ion-ion Coulomb collisions is distributed typically in the range 2−100 kpc (see Egan et al. 2016). The second model (CGL) allows for the development of anisotropy in the velocity thermal distribution (two-temperature approach), according to the conservation of the first adiabatic invariant (the magnetic momentum) of charged particles and the absence of heat conduction. The third model (BA) differs from the second by the inclusion of a phenomenological constraint on the temperature anisotropy due to the fast development of the firehose and mirror instabilities at the microscales (much smaller than the typical turbulence scales, reaching the ions kinetic scales). These instabilities are triggered by the temperature anisotropy itself.

Compared to the Faraday rotation maps resulting from the one-temperature collisional model (MHD), those from the collisionless CGL model present a relative dispersion smaller, with a steeper and less intense power spectrum in all scales. On the other hand, the statistical properties of the RM maps resulting from the collisionless BA model, which bounds the anisotropy to the firehose and mirror stable thresholds, are very similar to those of the MHD model.

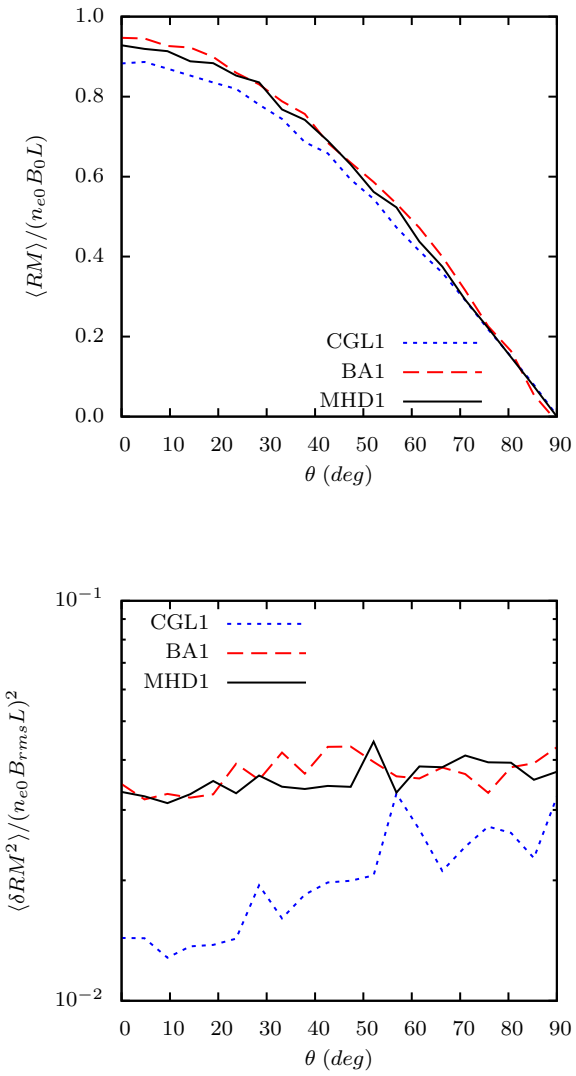

Figure 2. Normalized values of average (top) and dispersion (bottom) of the RM as a function of the angle θ between the line-of-sight and the uniform magnetic field.

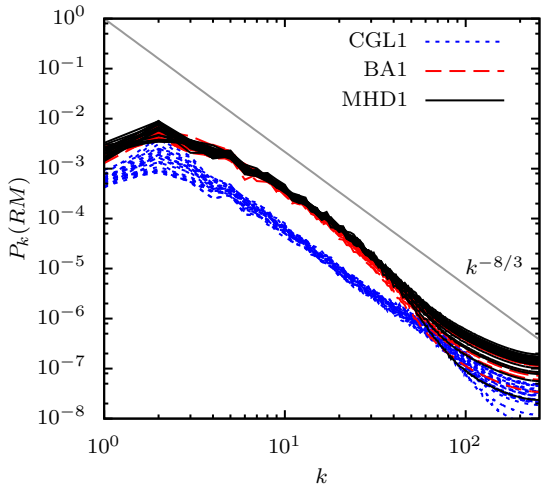

Figure 3. Power spectrum of the RM maps. The multiple lines presented for each model correspond to the power spectrum calculated for different angles θ between the line-of-sight and the uniform magnetic field, from $\theta = 0$ to $\theta = 90°$. A thin grey straight line with slope $-8/3$ is drawn for comparison.

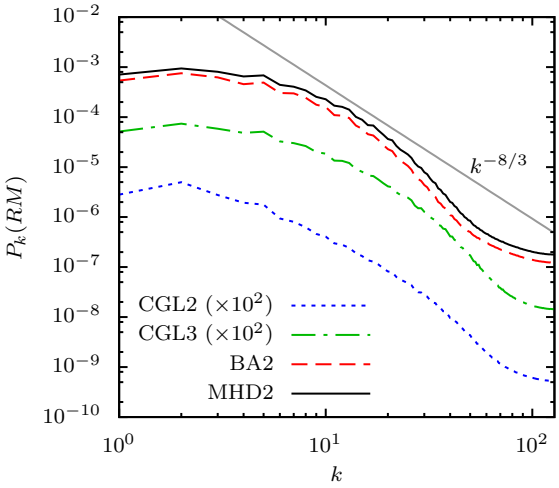

Figure 4. Same as in Figure 3, but for models $CGL2$, $CGL3$, $BA2$, and $MHD2$.

As stressed in Section 1, in Paper I we performed a similar RM analysis of collisionless two-temperature (with fixed values) models for the intracluster medium, but without considering the effects of the thermal relaxation by the kinetic instabilities. In this case the results were similar to those of the CGL model above, i.e., with significant differences in the RM maps and their statistical properties with regard to the collisional MHD model. Specifically, important imprints of the pressure anisotropy were found to prevail in the magnetic field structure resulting in Faraday rotation maps with smaller correlation lengths.

It has been demonstrated in SL+14 that the inclusion of the anisotropy relaxation by the kinetic mirror and firehose instabilities in collisionless two-temperature systems makes the statistical properties of the turbulence (in high β plasmas) as well as the amplification of the magnetic fields via the small-scale turbulent dynamo very similar to those of collisional MHD systems. The later approach is in fact used in most numerical simulations of the intracluster medium.

Therefore, the present result, *in principle*, reinforces the justification for the use of the collisional MHD approximation at least in studies of the large scale properties of the ICM. Nevertheless, this study has limitations and several questions still remain opened, as we briefly address below.

Recently Santos-Lima et al. (2016) have reviewed the limitations of the anisotropy relaxation approach employed, e.g., in SL+14. For instance, this neglects the effects of the microscale magnetic fields generated by microinstabil-

ities on the stretching rate of the large scale component (near the injection scale of the turbulence) (see also Schekochihin & Cowley 2006; Mogavero & Schekochihin 2014; Melville, Schekochihin, & Kunz 2016).

Furthermore, the present study has focussed only on the subsonic regime of the turbulence driven by purely solenoidal forcing, which explains the dominance of incompressible motions. On the other hand, the turbulence generated by the merging processes in the ICM is expected to be partially compressional (at the injection scales) and at least mildly supersonic (Brunetti & Jones 2014; Brüggen & Vazza 2015; Bykov et al. 2015) and, in fact, a compressible cascade in the ICM can reach small scales ($0.1 - 1$ kpc) before being dissipated. This implies that the magnetic fields can be entangled and/or advected also by compressive motions. In addition, weak shocks and collisionless effects will also affect the microphysics of processes like heating transport and thermal conduction (e.g., Santos-Lima et al. 2016), and may be important to the re-acceleration of particles in the ICM (see for example Brunetti & Lazarian 2007, 2011). The complex interplay between compressible modes (and shocks) and collisionless effects (as the collisionless damping) which have been neglected in the present collisionless MHD approach turn it inadequate to treat the compressible turbulent regime of the ICM (see further discussion on this subject in Santos-Lima et al. 2016).

ACKNOWLEDGEMENTS

RSL acknowledges support from a grant of the Brazilian Agency FAPESP (2013/15115-8), EMGDP partial support from FAPESP (2013/10559-5) and CNPq (306598/2009-4) grants. G.K. acknowledges support from FAPESP (grants no. 2013/04073-2 and 2013/18815-0) and PNPD/CAPES (grant no. 1475088) through a Postdoctoral Fellowship at University Cruzeiro do Sul. The numerical simulations in this work were carried out in the supercluster of the Astrophysical Informatics Laboratory (LAi) of IAG-USP and UnicSul whose purchase was made possible by FAPESP. The authors would also like to acknowledge the anonymous referee for the critics and suggestions which helped to improve this work.

REFERENCES

Beresnyak A., Miniati F., 2016, ApJ, 817, 127
Brüggen M., Vazza F., 2015, ASSL, 407, 599
Brunetti G., Jones T. W., 2014, IJMPD, 23, 1430007-98
Brunetti G., Lazarian A., 2011, MNRAS, 412, 817
Brunetti G., Lazarian A., 2007, MNRAS, 378, 245
Bykov A. M., Churazov E. M., Ferrari C., Forman W. R., Kaastra J. S., Klein U., Markevitch M., de Plaa J., 2015, SSRv, 188, 141
Chew G. F., Goldberger M. L., Low F. E., 1956, RSPSA, 236, 112
Egan H., O'Shea B. W., Hallman E., Burns J., Xu H., Collins D., Li H., Norman M. L., 2016, arXiv, arXiv:1601.05083
Enßlin T., Vogt C., Pfrommer C., 2005, mpge.conf, 231
Falceta-Gonçalves, D., & Kowal, G. 2015, ApJ, 808, 65
Feretti L., Dallacasa D., Giovannini G., Tagliani A., 1995, A&A, 302, 680
Gary S. P., 1993, tspm.book, 193
Kotarba H., Lesch H., Dolag K., Naab T., Johansson P. H., Donnert J., Stasyszyn F. A., 2011, MNRAS, 415, 3189
Kowal G., Falceta-Gonçalves D. A., Lazarian A., 2011, NJPh, 13, 053001
Kunz M. W., Schekochihin A. A., Stone J. M., 2014, PhRvL, 112, 205003
Melville S., Schekochihin A. A., Kunz M. W., 2016, MNRAS, 459, 2701
Mogavero F., Schekochihin A. A., 2014, MNRAS, 440, 3226
Nakwacki M. S., Kowal G., Santos-Lima R., de Gouveia Dal Pino E. M., Falceta-Gonçalves D. A., 2016, MNRAS, 455, 3702
Rincon F., Schekochihin A. A., Cowley S. C., 2015, MNRAS, 447, L45
Riquelme M. A., Quataert E., Verscharen D., 2015, ApJ, 800, 27
Santos-Lima R., de Gouveia Dal Pino E. M., Kowal G., Falceta-Gonçalves D., Lazarian A., Nakwacki M. S., 2014, ApJ, 781, 84
Santos-Lima R., Yan H., de Gouveia Dal Pino E. M., Lazarian A., 2016, MNRAS, 460, 2492
Schekochihin A. A., Cowley S. C., 2006, PhPl, 13, 056501
Sharma P., Hammett G. W., Quataert E., Stone J. M., 2006, ApJ, 637, 952
Sironi L., 2015, ApJ, 800, 89
Sironi L., Narayan R., 2015, ApJ, 800, 88

This paper has been typeset from a TEX/LATEX file prepared by the author.